DOI: 10.1002/aenm.201701623

Full Paper

Engineering temperature-dependent carrier concentration in bulk composite materials via temperature-dependent Fermi level offset

Si Hui, Wenpei Gao, Xu Lu, Anurag Panda, Trevor P. Bailey, Alexander A. Page, Stephen R. Forrest, Donald T. Morelli, Xiaoqing Pan, Kevin P. Pipe, and Ctirad Uher**

Dr. S. Hui

Department of Mechanical Engineering, Department of Physics, University of Michigan – Ann Arbor, Ann Arbor MI, 48109, USA

Dr. W. Gao

Department of Chemical Engineering and Materials Science, University of California – Irvine, Irvine CA, 92697, USA

Dr. X. Lu

Department of Chemical Engineering and Materials Science, Michigan State University, East Lansing MI, 48824, USA

A. Panda

Department of Materials Science and Engineering, University of Michigan – Ann Arbor, Ann Arbor MI, 48109, USA

T. P. Bailey

Department of Physics, University of Michigan – Ann Arbor, Ann Arbor MI, 48109, USA

Dr. A. A. Page

Department of Physics, University of Michigan – Ann Arbor, Ann Arbor MI, 48109, USA

Prof. S. R. Forrest

Department of Physics, Department of Materials Science and Engineering, Department of Electrical Engineering and Computer Science, University of Michigan – Ann Arbor, Ann Arbor MI, 48109, USA

Prof. D. T. Morelli

Department of Chemical Engineering and Materials Science, Department of Physics and Astronomy, Michigan State University, East Lansing MI, 48824, USA

Prof. X. Pan

Department of Chemical Engineering and Materials Science, Department of Physics and Astronomy, University of California – Irvine, Irvine CA, 92697, USA

Prof. K. P. Pipe

Department of Mechanical Engineering, Department of Electrical Engineering and Computer Science, University of Michigan – Ann Arbor, Ann Arbor MI, 48109, USA

Email: pipe@umich.edu

Prof. C. Uher

Department of Physics, University of Michigan – Ann Arbor, Ann Arbor MI, 48109, USA

Email: cuher@umich.edu

Keywords: thermoelectric materials, modulation doping, composite materials

Abstract Text:

Precise control of carrier concentration in both bulk and thin-film materials is crucial for many solid-state devices, including photovoltaic cells, superconductors, and high mobility transistors. For applications that span a wide temperature range (thermoelectric power generation being a prime example) the optimal carrier concentration varies as a function of temperature. In this work, we present a modified modulation doping method to engineer the temperature dependence of the carrier concentration by incorporating a nano-sized secondary phase that controls the temperature-dependent doping in the bulk matrix. We demonstrate this technique by de-doping the heavily defect-doped degenerate semiconductor GeTe, thereby enhancing its average power factor by 100% at low temperatures, and with no deterioration at high temperatures. This can be a general method to improve the average thermoelectric performance of many other materials.

1. Introduction

The performance metrics of many electronic device technologies depend on a carefully controlled charge carrier concentration.[1-11] However, the concentration that is optimal may be a strong function of temperature.[12] For example, the carrier concentration that maximizes the dimensionless thermoelectric figure of merit ZT (and thus the energy conversion efficiency) of a thermoelectric (TE) material varies depending upon the temperature, as illustrated in **Figure 1a** and **1b** and detailed Section 1 of the Supporting Information. ZT is defined as $ZT = S^2\sigma T/\kappa$, where S is the Seebeck coefficient, σ is electrical conductivity, T is temperature, and κ is thermal conductivity. This poses a challenge since TE devices are typically operated over a wide range of temperatures and, with a fixed carrier concentration, the performance obviously cannot be optimized at all temperatures. The problem is magnified by the fact that the figure of merit is strongly temperature dependent and is typically optimized by adjusting the carrier concentration near its peak value. Conventional doping strategies based on adding impurity atoms do not offer a means of controlling the temperature dependence of the carrier concentration because the ionization energy of the dopants is usually quite low such that essentially all are ionized at relatively low temperatures.[13,14] Moreover, limiting

the solubility and low doping efficiency of elements in a given matrix may also limit the concentration range that can be achieved.[15]

Various approaches have been proposed to enhance the average performance of thermoelectric materials. A high average thermoelectric figure of merit over a wide range of temperature has recently been realized in K-doped $PbTe_{0.7}S_{0.3}$ composites originating from a low thermal conductivity combined with a band-gap opening at elevated temperatures.[16] Another example is heavily doped *p*-type single crystals of SnSe that benefit from the increased number of band pockets near the Fermi level.[17] Attempts to achieve temperature-dependent doping have also been made, such as exploring the temperature-dependent solubility of Ag in the PbTe matrix[12] and studying the temperature-dependent dopant migration in multiphase $(PbTe)_{0.65}(PbS)_{0.25}(PbSe)_{0.1}$ composites.[18] However, all these examples critically depend on a specific material property (e.g., temperature-dependent bandgap opening, multi-carrier pocket band structure, and temperature-dependent solubility) thus severely constraining their application to a wide range of materials. While highly desirable, a more general temperature-dependent doping method has, to our knowledge, not yet been proposed.

A unique doping method is modulation doping,[19] first demonstrated in GaAs-$Al_xGa_{1-x}As$ heterojunction superlattices by Dingle et al. By intentionally separating doped regions from transport pathways, charge carrier mobilities in modulated structures can attain exceptionally high values. Modulation doping has been used in achieving a very high mobility of two-dimensional electron gas (2DEG) by inserting a single-unit-cell insulating layer,[20] in photoinduced modulation doping in graphene/boron nitride heterojunctions,[21] in quasi-one-dimensional Ge-Si_xGe_{1-x} core-shell nanowire electron systems with enhanced mobility,[22] and in *p*-type CdS nanowires with high hole

mobility for photovoltaic applications.[23] In addition to the low dimensional structures and devices, modulation doping has recently been demonstrated as an effective method for enhancing the carrier mobility in 3-dimensional bulk materials, especially those intended for thermoelectric applications.[24-27] In spite of these successes, to the best of our knowledge no temperature-dependent doping scheme based on modulation doping has been demonstrated.

Inspired by modulation doping which utilizes the Fermi energy offset between two neighboring regions to promote charge carrier transfer, we examine the prospect of temperature tuning such offsets to realize a temperature-dependent carrier concentration. This is achieved by creating nanoscale inclusions of a secondary phase that has a temperature dependent Fermi energy which is significantly different from that of the bulk, offering a means for tuning the bulk carrier concentration. In this work, we demonstrate the technique in a GeTe-$CuInTe_2$ composite structure. Since incorporating a secondary phase in the matrix is not restricted by a solubility limit or doping efficiency, the choice of the compounds (secondary phase materials) is much larger than that of conventional dopants, and thus this method potentially encompasses a large pool of candidate materials to which it can be applied.

Details concerning the synthesis of our composite materials, their structural characterization and techniques of transport property measurements are given in Section 4. Here we note that the composite structures were of the form $(Ge_2Te_2)_x(CuInTe_2)_{1-x}$, where x = 100, 98, 95, 90, 87.5, 85, 70, 30, and 10. The structures are designated as GT-x. For instance, GT-90 stands for $(Ge_2Te_2)_{90}(CuInTe_2)_{10}$.

2. Results and Discussion

While numerous material aspects can contribute to a temperature-dependent carrier concentration (e.g., phase transition or a temperature-dependent band structure), charge transfer at interfaces proceeds with highly temperature tunable Fermi energies. The resulting band bending and charge transfer, including their dependence on the Fermi energy, can be quantitatively described by self-consistent solutions of the drift-diffusion and Poisson equations.

We have numerically solved a 3-dimensional spherically symmetric interface charge transfer problem using a fourth-order Runge-Kutta algorithm with the shooting method.[28] Details of the model are given in Section 2 of the Supporting Information.

The band bending and charge distribution profiles, together with the average carrier concentration change in the matrix, depend on many parameters, including the Fermi level offset, band structure, dielectric constant of each phase, electrostatic potential drop across the interface, original carrier concentration in each phase, size of the secondary phase inclusions, and secondary phase volume fraction, all of which have been taken into account. Other parameters not included in the model, such as surface states, charge accumulation, and the non-spherical shape of inclusions may also influence the results. Here, we focus on the parameters that significantly change in the GeTe-$CuInTe_2$ system, such as the Fermi level offset, secondary inclusion size, secondary phase volume fraction, and inclusion shape. The average bulk matrix carrier concentration change, which depends on the shape, size, and molar concentration of the secondary phases is shown in **Figure 2a** and **2b**. It is worth noting that forming nano-size instead of micro-size secondary phases is crucial to altering the carrier concentration in heavily doped materials, since the depletion width decreases as the

carrier concentration increases. Moreover, the surface-to-volume ratio of the secondary phase inclusions can have a significant influence.

As an example of how charge transfer at interfaces can induce a temperature-dependent carrier concentration, we consider a typical heterojunction shown in the inset of **Figure 2c**. The secondary phase material has a much weaker temperature-dependent Fermi energy due to a temperature-independent band structure, and the matrix material has a temperature-dependent band convergence, such as found in group IV-VI compounds.[14,29] As temperature increases, the Fermi level offset decreases. The convergence of the Fermi energies significantly alters the charge transfer across the interface and thus the average bulk matrix carrier concentration, shown in **Figure 2c** and **2d**.

The GeTe matrix is a degenerately self-doped semiconductor with carrier concentration ~8×10^{20} cm^{-3}. It has a rhombohedral structure at room temperature.[30] GeTe is characterized by a relatively high power factor at high temperatures due to the convergence of the two valence bands, but also a relatively poor performance at lower temperatures due to its high carrier concentration.[29,31] On the other hand, the ternary chalcopyrite with a tetragonal structure, $CuInTe_2$, with a low carrier concentration of ~10^{18} cm^{-3}, has drawn attention for its potential thermoelectric applications due to its low thermal conductivity.[32] Density functional theory (DFT) calculations were performed to obtain the band structure of $CuInTe_2$ at T=0.[33,34] Based on the calculated band structure, high-temperature transport properties were calculated by solving the Boltzmann transport equation and assuming that the band structure is temperature-independent. The calculated transport properties agree with the experimental results, supporting the assumption of a temperature-independent band

structure for $CuInTe_2$.[33,34] We selected this compound as the secondary phase de-dopant because of its more rigid band structure with respect to temperature, compared to that of GeTe.

The dissimilar crystal structures of GeTe and $CuInTe_2$ result in both micro- and nano-scale segregation of $CuInTe_2$, as corroborated by energy dispersive X-ray spectroscopy (EDS) mapping and transmission electron microscopy (TEM) shown in **Figure 3a** and **3b** (Details regarding the density, X-ray diffraction (XRD), and scanning electron microscopy (SEM) provided in Section 3 of the Supporting Information). It is worth noting that the XRD, EDS mapping, and SEM results all indicate that only GeTe and $CuInTe_2$ form as the major phases. EDS mapping and SEM also confirm the distribution of micron-size inclusions is homogeneous. Observations of nanoscale $CuInTe_2$ inclusions in multiple randomly selected regions confirm the existence, size, and shape of the $CuInTe_2$ secondary phases, shown as **Figure 3b, 3c,** and **3d**.

We also performed EDS 2D mapping and a line scan that corroborate the nanoscale size and distribution of the $CuInTe_2$ inclusions in the matrix, as shown in **Figure 3e**. The room temperature Fermi level offset between GeTe and $CuInTe_2$ bulk is 0.3 ± 0.2 eV as determined from the onset of the ultraviolet photoemission spectroscopy (UPS) in the low kinetic energy range, **Figure 4a**. The onset energy of the UPS spectrum of the composite with 5% $CuInTe_2$ shifts by 0.2 eV from GeTe to $CuInTe_2$, suggesting band bending caused by the high interface density.[35] Here the interface density is defined as the total area of the interface per unit volume. This shift is also observed in the X-ray photoemission spectroscopy (XPS) core levels, shown as **Figure 4b**.

The transport properties of GeTe-$CuInTe_2$ composites from room temperature to 800 K are consistent with the carrier concentration depletion model, as shown in **Figure 5a-c**. The transport

properties of pure GeTe are similar to those measured previously.[29] Temperature-dependent Fermi energies in pure GeTe and $CuInTe_2$ were derived by fitting their temperature-dependent transport coefficients as shown in the inset of Figure 5a, with details found in Section 1 of the Supporting Information. The temperature dependence of the Fermi energy in GeTe is stronger than in $CuInTe_2$. This is due to the band convergence of the GeTe light valence *L* band and heavy *Σ* band. Indeed, the large Fermi level offset of approximately 0.3 eV at room temperature shrinks to nearly zero at 600 K, resulting in significantly weakened band bending near the interface, which follows the mechanism in Figures 2c and 2d. The disappearance of the Fermi energy offset between the GeTe and $CuInTe_2$ phases at 600 K causes an anomalous decrease of the Seebeck coefficient, an increase in the electrical conductivity, and an increase of the carrier concentration. The Fermi energy offset at temperatures below 600 K depletes the carriers in the GeTe matrix, which results in the reduced carrier concentration, electrical conductivity, and an enhanced Seebeck coefficient. The carrier depletion at lower temperatures pushes the carrier concentration in the GeTe matrix closer to the optimal value (the carrier concentration value that maximizes the power factor) for that temperature and thus enhances the power factor. As the Fermi energy offset collapses at higher temperatures, the doping effect ceases to influence the high temperature transport properties. An enhanced average power factor is achieved in both GT-95 and GT-90 samples, shown in **Figure 5d**, consistent with the prediction shown as the blue dots in Figure 1b.

It is necessary to exclude several possible artifacts that influence the transport properties in the same manner as the doping effects near room temperature. Possible scenarios include: 1. Cu and In in the GeTe matrix fills the defect sites and thus reduces the carrier concentration; 2. energy filtering caused by the micron-size and nano-size $CuInTe_2$ inclusions can enhance the Seebeck coefficient

while decreasing the electrical conductivity and carrier concentration; 3. strain caused by the $CuInTe_2$ precipitates affects the transport properties of the GeTe matrix; and 4. interface states can reduce the carrier concentration in the GeTe matrix.

Segregation of $CuInTe_2$ in GT-98 as observed in the backscattered electron (BSE) image and a 15 K decrease of the phase transition temperature in all composites compared to pure GeTe, as determined by heat capacity measurements, confirm that the solubility of Cu and In in the GeTe matrix is below 2%, shown in **Figure 6a** and **Figure S2a**. Moreover, the room temperature mobility of the GeTe-$CuInTe_2$ composites can be described by scattering from 1% impurities and nano-scale segregates (see Section 4 of the Supporting Information). The mobility of the composites studied here is significantly larger than for impurity-doped GeTe alloys, such as GeTe-In_2Te_3 alloys.[31] Similarly, the influence of 2% $CuInTe_2$ on the room temperature transport properties is less than that caused by 5% $CuInTe_2$, shown in Figure 6c. These observations address the first potential artifact: Cu and In dissolved in the GeTe matrix do not adequately account for the reduced carrier density at room temperature.

Scattering from nano-scale inclusions has an $E^{3/2}$ energy dependence, whereas scattering by defects and acoustic phonons follows an $E^{-1/2}$ dependence.[14] Changing the energy dependence of mobility can enhance the Seebeck coefficient. In this work, scattering by nano-scale inclusions contributes only a negligible amount to the total charge carrier scattering (**Figure 6b**), and hence a negligible amount to the mobility. Rather than scattering, micron-scale inclusions block low energy carriers, and the enhanced average energy of the charge carriers increases the Seebeck coefficient. However, the increasing number and size of $CuInTe_2$ micro-grains reduces the electrical conductivity and does not enhance the Seebeck coefficient, as shown in **Figure 6c**. This suggests that $CuInTe_2$ inclusions

block carriers of all energies, consistent with the room temperature band alignment. Thus, we rule out the possibility that the room temperature transport properties change as a result of energy filtering. Moreover, TEM analysis shows that the strain within the matrix fluctuates by only 1-2%, as shown in **Figure 6d**. Such small fluctuations are unlikely to cause any dramatic changes in the carrier concentration. Finally, the estimated matrix carrier concentration reduction caused by the interface states is insufficient to account for the measured matrix carrier concentration reduction. Details are provided in the Supporting Information.

3. Conclusion

In summary, we demonstrate a general method whereby the carrier concentration can be adjusted within a large temperature range to enhance the average thermoelectric performance. The temperature-dependent doping mechanism is based on incorporating nano-size secondary phases with appropriate Fermi energy offsets, which can be realized in a diverse class of materials. Reduced scattering from nano-size precipitates compared to elemental impurities results in a higher mobility of charge carriers than conventional doping. The close relationship between the matrix carrier density and the Fermi level offset facilitates other possible methods (e.g. phase transition, strain, magnetic field, etc.) to control the carrier density. The extension of this mechanism from bulk materials to thin film structures is straightforward, and could support applications in the field of photovoltaics, optics, electronics, and even superconductors.

4. Experimental Section

Synthesis: Raw elements of germanium, copper, indium, and tellurium were purchased from Alfa Aesar with the following purities: Ge (pieces, 99.9999+%), Cu (shot, 99.98%), In (ingots, 99.9999+%), and Te (lumps, 99.999+%). The starting materials were weighed according to the stoichiometric ratio $(Ge_2Te_2)_x(CuInTe_2)_{100-x}$ with x=100, 98, 95, 90, 87.5, 85, 70, 30, and 10 in the glovebox under an argon atmosphere with oxygen and water levels below 0.1 ppm and 0.5 ppm, respectively. In this paper, the samples are denoted as GT-x, where x represents the molar concentration of GeTe in the sample. The weighed materials were then put in carefully cleaned quartz ampoules and sealed under a pressure of less than 10^{-4} Torr and placed in a furnace heated according to the following schedule: slow heating up to 1000°C at the rate of 1.5°C/min; rest at 1000°C for 12 hours; slow cooling down to 600°C at 2°C/min; annealing at 600°C for 4 days; and finally slow cooling down to room temperature at 2°C/min. The as-cast ingots were hand-milled to powders under argon atmosphere and hot-pressed at a temperature of ~500°C under a pressure of ~60 MPa for 30 min.

Powder X-ray Diffraction: GT-x samples were ground to fine powders and placed into aluminum holders for room temperature powder X-ray diffraction (PXRD) measurements using a Rigaku Ultima IV X-Ray Diffractometer utilizing a 2.2 kW Cu K-α radiation. The diffraction signal was collected from 5° to 90° at the rate of 2°/min with 0.05° steps. The measured peaks were compared with the peaks of the known compound from the reference library to identify the phases present.

Transport property measurements: 10 mm × 3 mm × 3 mm bars were cut from the hot pressed pellets for high temperature Seebeck coefficient and electrical conductivity measurements. Both the high temperature (from room temperature to 800 K) and low temperature (from 80 K to room

temperature) transport properties were measured using homemade setups. For high temperature Hall measurements, bar-shaped samples were cut with dimensions of 8 mm × 3 mm × 1 mm. The high temperature Hall coefficient was measured using homemade equipment with a superconducting magnet. For high temperature thermal conductivity studies, we used disk-shaped samples with 10 mm diameter and 1 mm thickness. The thermal conductivity was computed from the equation $\kappa = \lambda \times C_p \times \rho$, where κ, λ, C_p, and ρ represent the thermal conductivity, thermal diffusivity, specific heat capacity, and density, respectively. Measurements of the thermal diffusivity were made using an Anter Flashline 3000 laser flash system, specific heat capacity was determined with the aid of the Pegasus 404 Differential Scanning Calorimeter (DSC) from Netzsch, and the density of the pellets was established by the Archimedes method.

Electron microprobe measurements: Composition mapping and surface topography of the samples were characterized with the help of energy dispersive spectroscopy (EDS), backscattered electron microscopy (BSE), and secondary electron microscopy implemented within a FEI Helios 650 Dualbeam Focussed Ion Beam Workstation and Scanning Electron Microscope (SEM) on carefully polished samples. Transmission electron microscopy (TEM) imaging was carried out on Titan S/TEM at 300 kV at the Center of Nanophase Materials Science at Oak Ridge National Laboratory.

Ultraviolet and X-ray Photoemission Spectroscopy: Photoemission spectroscopy measurements were carried out in an ultrahigh-vacuum chamber with pressure < 1×10^{-9} Torr, using the 21.22 eV Helium-I (Ultraviolet) and 1486.7 eV Aluminum-K_α (X-ray) emissions. The samples were polished and stored under an environment of Ar to prevent the oxidation of the surface before transferring into the system through a N_2-filled glovebox. The spectra were collected using a hemispherical electron energy analyzer (Thermo VG). To minimize sample charging, electrical contact was maintained *via* a

metal clip attached to a copper puck connected to ground. The sample was biased at -9.00 V to ensure collection of low kinetic energy electrons.

Supporting Information

Supporting Information is available from the Wiley Online Library or from the author.

Acknowledgements

Financial support for this investigation was provided by the U. S. Department of Energy (DOE)- U. S.-China Clean Energy Research Center (CERC-CVC) under the Award No. DE-PI0000012. The hot-pressing process at Michigan State University was supported as part of the Center for Revolutionary Materials for Solid State Energy Conversion, an Energy Frontier Research Center, funded by the U. S. Department of Energy, Office of Science, Office of Basic Energy Sciences, under the Award No. DE-SC0001054. Financial support for UPS and XPS was provided by U.S. Army Research Office (S. R. Forrest and A. Panda). Financial support for the BSE, SEM, and EDS was provided by the College of Engineering, University of Michigan. W. Gao was supported by the National Science Foundation with the grant number CBET-1159240 and School of Engineering at University of California, Irvine. TEM imaging and analysis were carried out at Irvine Materials Research Institute at the University of California, Irvine, and the Center of Nanophase Materials Sciences at Oak Ridge National Laboratory (ORNL). We would like to thank Dr. Miaofang Chi for TEM imaging and analysis at ORNL, and P. Gao

and T. P. Hogan for their confirmation measurement of thermal diffusivity and heat capacity at Michigan State University. S. Hui also thanks H. Sun and H. Chi for helpful discussions.

Received: ((will be filled in by the editorial staff))
Revised: ((will be filled in by the editorial staff))
Published online: ((will be filled in by the editorial staff))

References

[1] J. M. Luther, P. K. Jain, T. Ewers, A. P. Alivisatos, *Nat. Mater.* **2011**, *10*, 361.

[2] A. Boltasseva, H. A. Atwater, *Science* **2011**, *331*, 290.

[3] X. Z. Lan, S. Masala, E. H. Sargent, *Nat. Mater.* **2014**, *13*, 233.

[4] M. Graetzel, R. A. J. Janssen, D. B. Mitzi, E. H. Sargent, *Nature* **2012**, *488*, 304.

[5] N. M. Gabor, J. C. W. Song, Q. Ma, N. L. Nair, T. Taychatanapat, K. Watanabe, T. Taniguchi, L. S. Levitov, P. Jarillo-Herrero, *Science* **2011**, *334*, 648.

[6] J. Wu, O. Pelleg, G. Logvenov, A. T. Bollinger, Y. J. Sun, G. S. Boebinger, M. Vanevic, Z. Radovic, I. Bozovic, *Nat. Mater.* **2013**, *12*, 877.

[7] A. Gozar, G. Logvenov, L. F. Kourkoutis, A. T. Bollinger, L. A. Giannuzzi, D. A. Muller, I. Bozovic, *Nature* **2008**, *455*, 782.

[8] M. H. Whangbo, C. C. Torardi, *Science* **1990**, *249*, 1143.

[9] C. Richter, H. Boschker, W. Dietsche, E. Fillis-Tsirakis, R. Jany, F. Loder, L. F. Kourkoutis, D. A. Muller, J. R. Kirtley, C. W. Schneider, J. Mannhart, *Nature* **2013**, *502*, 528.

[10] A. Ohtomo, H. Y. Hwang, *Nature* **2004**, *427*, 423.

[11] S. Thiel, G. Hammerl, A. Schmehl, C. W. Schneider, J. Mannhart, *Science* **2006**, *313*, 1942.

[12] Y. Z. Pei, A. F. May, G. J. Snyder, *Adv. Energy Mater.* **2011**, *1*, 291.

[13] R. Enderlein, N. J. M. Horing, *Fundamentals of Semiconductor Physics and Devices*, World Scientific, Singapore, **1997**.

[14] Y. I. Ravich, B. A. Efimova, I. A. Smirnov, *Semiconducting Lead Chalcogenides*, Plenum, New York, **1970**.

[15] S. Hui, M. D. Nielsen, M. R. Homer, D. L. Medlin, J. Tobola, J. R. Salvador, J. P. Heremans, K. P. Pipe, C. Uher, *Journal of Applied Physics* **2014**, *115*, 103704.

[16] H. J. Wu, L. D. Zhao, F. S. Zheng, D. Wu, Y. L. Pei, X. Tong, M. G. Kanatzidis, J. Q. He, *Nat. Commun.* **2014**, *5*, 4515.

[17] K. L. Peng, X. Lu, H. Zhan, S. Hui, X. D. Tang, G. W. Wang, J. Y. Dai, C. Uher, G. Y. Wang, X. Y. Zhou, *Energ. Environ. Sci.* **2016**, *9*, 454.

[18] S. A. Yamini, D. R. G. Mitchell, Z. M. Gibbs, R. Santos, V. Patterson, S. Li, Y. Z. Pei, S. X. Dou, G. J. Snyder, *Adv. Energy Mater.* **2015**, *5*, 1501047.

[19] R. Dingle, H. L. Stormer, A. C. Gossard, W. Wiegmann, *Applied Physics Letters*, **1978**, *33*, 665.

[20] Y. Z. Chen, F. Trier, T. Wijnands, R. J. Green, N. Gauquelin, R. Egoavil, D. V. Christensen, G. Koster, M. Huijben, N. Bovet, S. Macke, F. He, R. Sutarto, N. H. Andersen, J. A. Sulpizio, M. Honig, G. E. D. K. Prawiroatmodjo, T. S. Jespersen, S. Linderoth, S. Ilani, J. Verbeeck, G. Van Tendeloo, G. Rijnders, G. A. Sawatzky, N. Pryds, *Nat. Mater.* **2015**, *14*, 801.

[21] L. Jun, J. Velasco, E. Huang, S. Kahn, C. Nosiglia, H. Z. Tsai, W. Yang, T. Taniguchi, K. Watanabe, Y. Zhang, G. Zhang, M. Crommie, A. Zettl, F. Wang, *Nat. Nanotechnol*. **2014**, *9*, 348.

[22] D. C. Dillen, K. Kim, E. S. Liu, E. Tutuc, *Nat. Nanotechnol.* **2014**, *9*, 116.

[23] F. Z. Li, L. B. Luo, Q. D. Yang, D. Wu, C. Xie, B. Nie, J. S. Jie, C. Y. Wu, L. Wang, S. H. Yu, *Adv. Energy Mater.* **2013**, *3*, 579.

[24] D. Wu, Y. L. Pei, Z. Wang, H. J. Wu, L. Huang, L. D. Zhao, J. Q. He, *Adv. Funct. Mater.* **2014**, *24*, 7763.

[25] Y. L. Pei, H. J. Wu, D. Wu, F. S. Zheng, J. Q. He, *J. Am. Chem. Soc.* **2014**, *136*, 13902.

[26] B. Yu, M. Zebarjadi, H. Wang, K. Lukas, H. Z. Wang, D. Z. Wang, C. Opeil, M. Dresselhaus, G. Chen, Z. F. Ren, *Nano. Lett.* **2012**, *12*, 2077.

[27] M. Zebarjadi, G. Joshi, G. H. Zhu, B. Yu, A. Minnich, Y. C. Lan, X. W. Wang, M. Dresselhaus, Z. F. Ren, G. Chen, *Nano. Lett.* **2011**, *11*, 2225.

[28] S. V. Faleev, F. Leonard, *Physical Review B*, **2008**, *77*, 214304.

[29] D. Wu, L. D. Zhao, S. Q. Hao, Q. K. Jiang, F. S. Zheng, J. W. Doak, H. J. Wu, H. Chi, Y. Gelbstein, C. Uher, C. Wolverton, M. Kanatzidis, J. Q. He, *J. Am. Chem. Soc.* **2014**, *136*, 11412.

[30] J. Goldak, C. S. Barrett, D. Innes, W. Youdelis, *J. Chem. Phys.* **1966**, *44*, 3323.

[31] H. Sun, X. Lu, H. Chi, D. T. Morelli, C. Uher, *Phys. Chem. Chem. Phys.* **2014**, *16*, 15570.

[32] R. H. Liu, L. L. Xi, H. L. Liu, X. Shi, W. Q. Zhang, L. D. Chen, *Chem. Commun.* **2012**, *48*, 3818.

[33] B. Wang, H. Xiang, T. Nakayama, J. Zhou, B. Li, *Physical Review B* **2017**, *95*, 035201.

[34] D. P. Rai, Sandeep, A. Shankar, A. P. Sakhya, T. P. Sinha, P. Grima-Gallardo, H. Cabrera, R. Khenata, M. P. Ghimire, R. K. Thapa, *Journal of Alloys and Compounds* **2017**, *699*, 1003.

[35] Z. Zhang, J. T. Yates, *Chem. Rev.* **2012**, *112*, 5520.

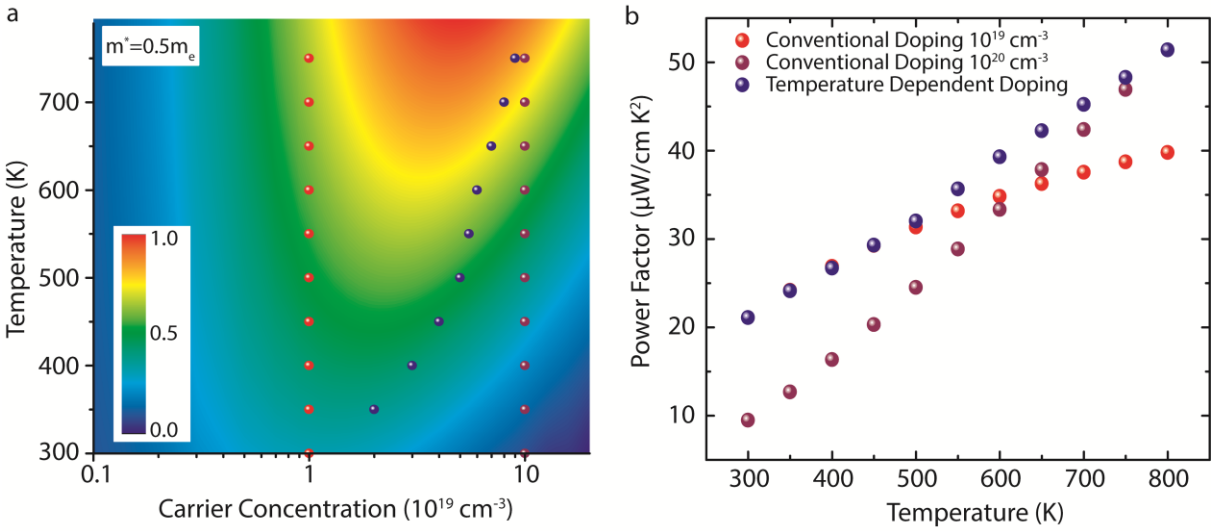

Figure 1. a: Normalized power factor as a function of carrier concentration and temperature for a single parabolic band with effective mass of 0.5 m_e. Blue spheres represent a temperature-dependent carrier concentration. The red and purple spheres represent temperature-independent carrier concentrations optimizing the power factor at low temperature and high temperature,

respectively. **b**: Temperature-dependent power factor corresponding to the three sets of spheres shown in **a**. Numerical results indicate that a varying carrier concentration is desired to enhance the average power factor over the wide temperature range. The conventional impurity doping method can only optimize the power factor at one particular temperature.

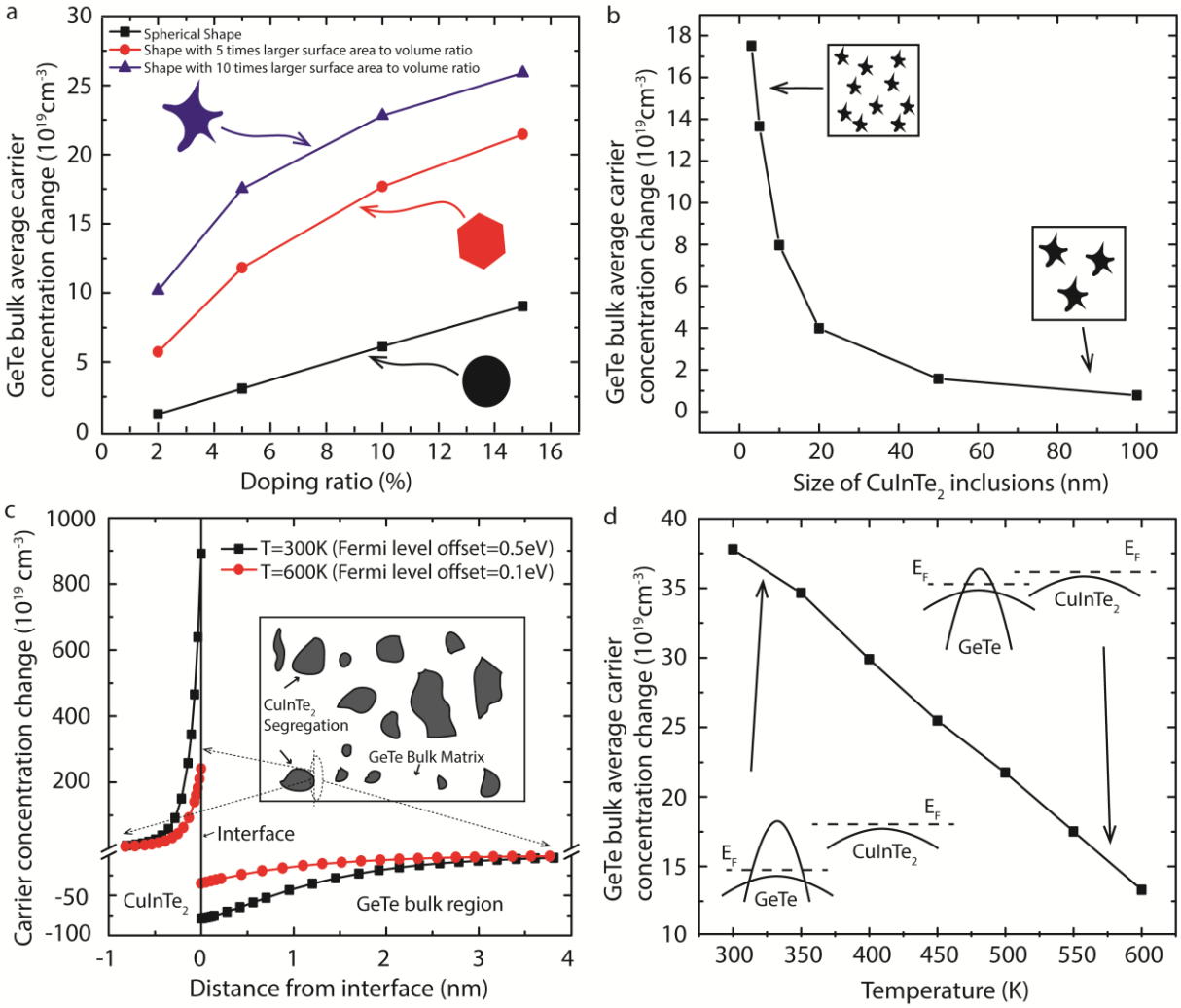

Figure 2. a: Average room temperature carrier concentration depletion over the bulk region as a function of secondary phase concentration with various secondary phase geometries of different surface- to- volume ratio. (The size of the secondary phase is set to be 3 nm) **b**: Average room temperature carrier concentration depletion over the bulk region as a function of the size of $CuInTe_2$ inclusions. (The doping ratio is set to be 5 mol% and the surface-to-volume ratio is set to be 10 times larger than that of spheres) **c**: Carrier concentration change profile at 300 K and 600 K near the

interface between GeTe and $CuInTe_2$ phases solved by our model. Here, we set the Fermi energy offset between the matrix and the secondary phase to be 0.5 eV at room temperature and 0.1 eV at 600 K, corresponding to the Fermi energy convergence in the GeTe-$CuInTe_2$ system. The material-wise fixed parameters are taken from the literature for the specific two materials we are using in this paper. Inset: 2D schematic for the distribution of secondary phase segregations in the matrix of the novel doping mechanism. **d**: Average carrier concentration depletion over the bulk region as a function of temperature assuming the Fermi level offset is a linear function of temperature. Important parameters are set as: a secondary phase segregation surface-to-volume ratio of 10:1 and a molar concentration of $CuInTe_2$ as 5%.

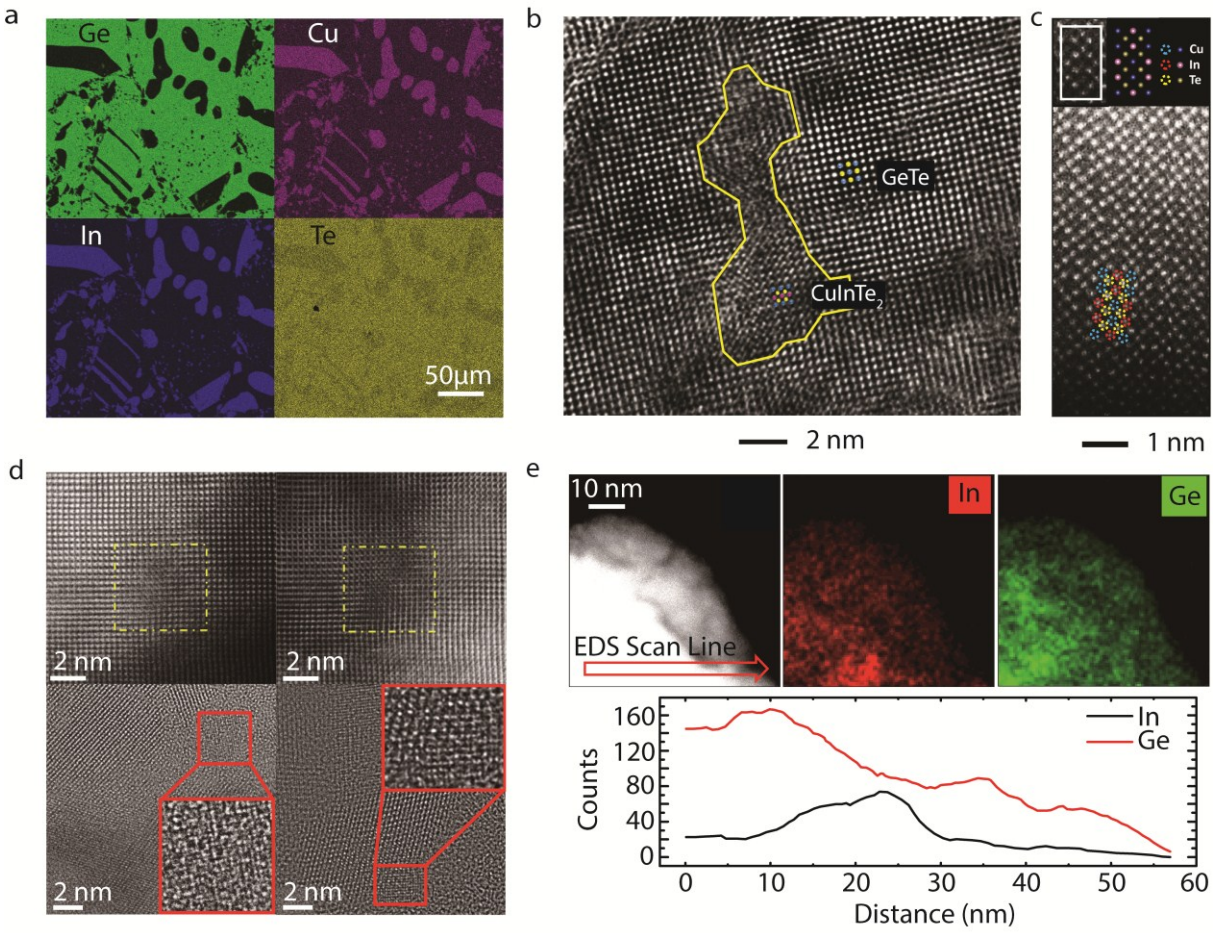

Figure 3. a: EDS mapping of Ge, Cu, In, and Te elements in the GT-70 sample, which contains 30% of $CuInTe_2$. Light regions represent the accumulation of the corresponding element. **b**: High resolution TEM image of a small region of the GT-70 sample. The large matrix bears a rhombohedral GeTe

structure, well fitted with the overlaid GeTe atomic model. In the matrix, the highlighted area shows an atomic lattice corresponding to the chalcopyrite $CuInTe_2$ structure, confirming the existence of the nano-size $CuInTe_2$ secondary phase. The shape of these nano-size segregations is not spherical. **c**: High angle annular dark field (HAADF) STEM Z-contrast image of a $CuInTe_2$ region, atomic columns of Cu, In and Te are identified by the intensity corresponding to the atomic number of each element. **d**: The top 2 images are *z*-contrast and bright field STEM image of GT-95 sample. The $CuInTe_2$ inclusion is highlighted in the yellow box. The bottom 2 images are high resolution TEM images of GT-95. Small areas of $CuInTe_2$ are highlighted and zoomed-in in the red boxes. **e**: EDS mapping of the Ge and In in GT-95, the HAADF image is in Grey scale, Ge map is in Green scale, and In map is Red scale. The red arrow indicates EDS line scan position and direction. The local In and Ge variation shows the distribution of the nanoscale $CuInTe_2$ inclusions.

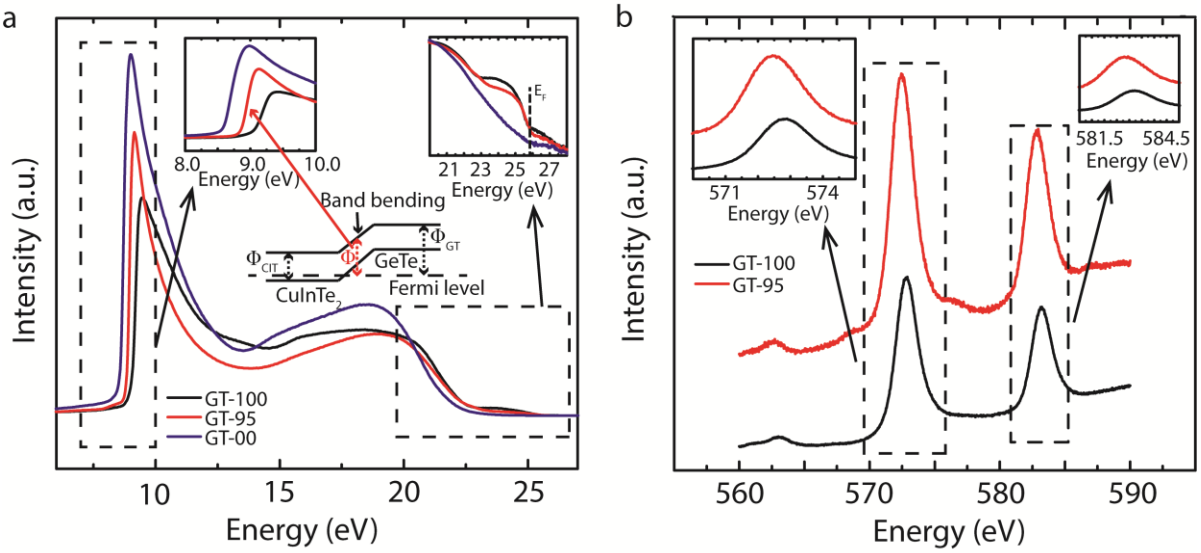

Figure 4. a: UPS results for the GT-100, GT-95, and GT-00 samples. The work function shift shown in the GT-95 sample suggests the interface density is high since the Fermi level is a spatial constant and the local vacuum level bends with the band bending, as illustrated in the middle inset. The top insets are the spectroscopy data focusing on the lower (left) and higher (right) kinetic energy range. The right inset verifies that the Fermi levels of the tested 3 samples are all aligned with the measurement system during the measurement, calibrated by measuring Fermi step of a freshly deposited Au film. **b**: XPS Te-3d core levels. The insets show the energy shift of the two peaks.

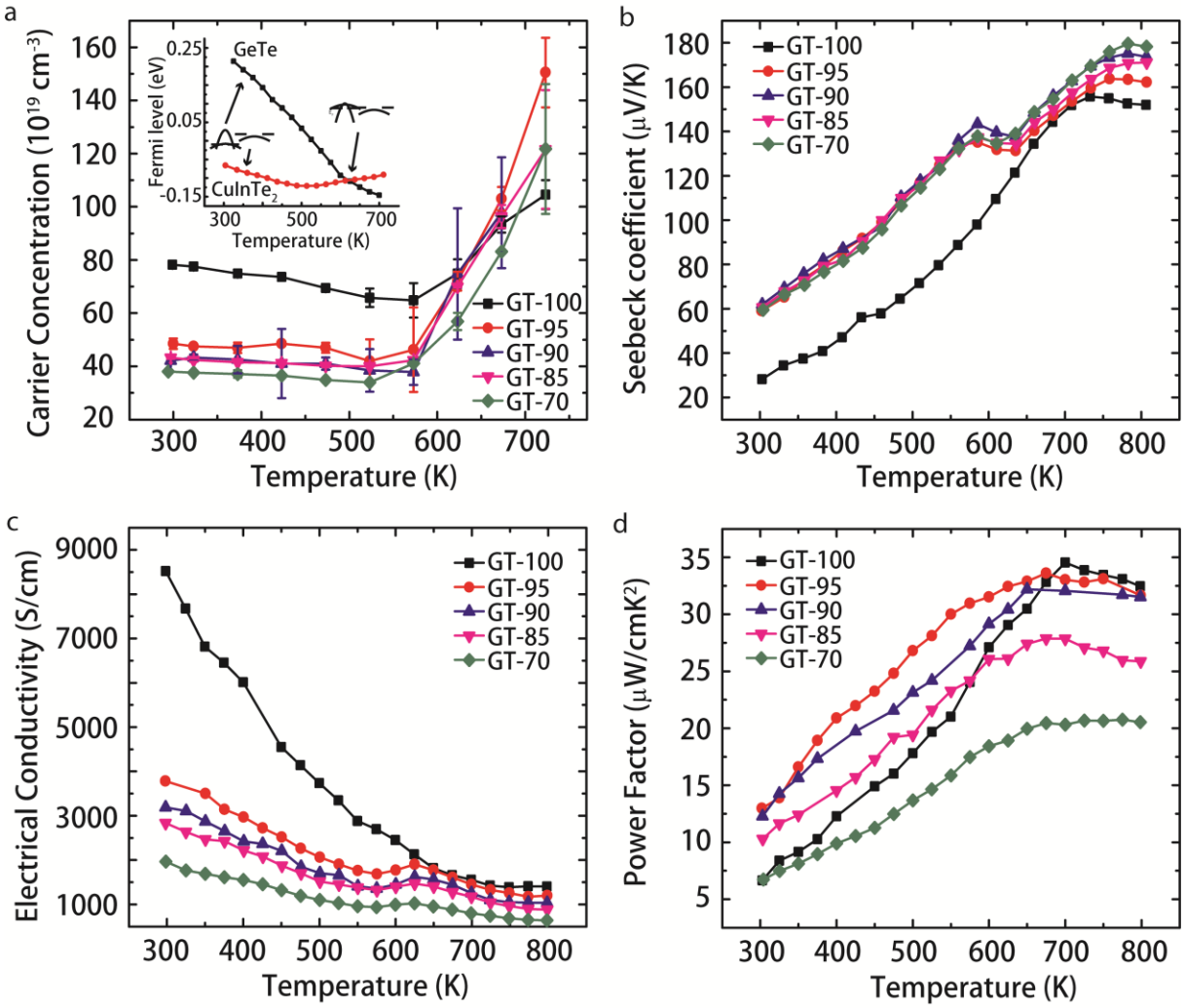

Figure 5. **a-c**: Temperature-dependent carrier concentration, Seebeck coefficient, and electrical conductivity of the GT-100, GT-95, GT-90, GT-85, and GT-70 samples. The inset in 5**a** shows the temperature-dependent Fermi energies of the pure GeTe and $CuInTe_2$, obtained by fitting the transport coefficients. The room-temperature offset was set to be 0.3eV based on the results of UPS. **d**: Temperature-dependent thermoelectric power factor of GT-100, GT-95, GT-90, GT-85, and GT-70 samples.

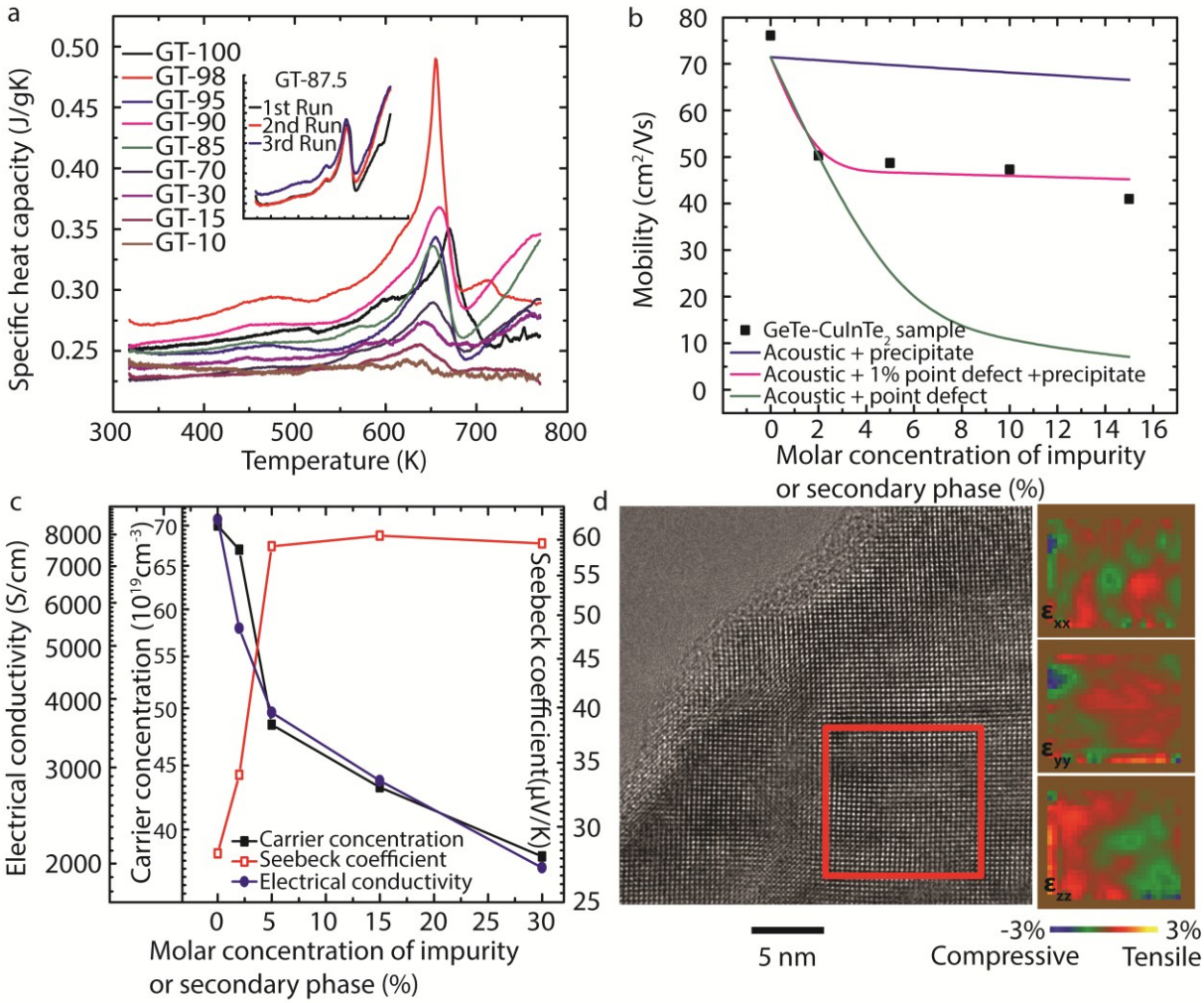

Figure 6 a: Temperature-dependent specific heat capacity of GT-*x* (with *x*=100, 98, 95, 90, 85, 70, 30, 15, and 10) samples. Results of 3 consecutive measurements on the GT-87.5 sample are shown in the inset of Fig. 6a. **b**: Room temperature mobilities as a function of the molar concentration of the impurity or the secondary phase in GeTe-$CuInTe_2$ from this work. The mobility calculated for various scattering mechanisms is represented as solid lines. **c**: Room temperature carrier concentration, Seebeck coefficient, and electrical conductivity as a function of the molar concentration of the secondary phase. **d**: Strain mapping of the GeTe matrix at various distance away from the segregated secondary phase obtained from a high resolution TEM image.

Temperature-dependent modulation doping is demonstrated in this study in the GeTe-$CuInTe_2$ composite material. Temperature-dependent carrier concentration is achieved by controlling the temperature-dependent Fermi level offset between a GeTe matrix and $CuInTe_2$ inclusions. An enhanced average power factor over a wide temperature range is demonstrated.

Keywords: thermoelectric materials, modulation doping, composite materials

Si Hui, Wenpei Gao, Xu Lu, Anurag Panda, Trevor P. Bailey, Alexander A. Page, Stephen R. Forrest, Donald T. Morelli, Xiaoqing Pan, Kevin P. Pipe, and Ctirad Uher**

Title: Engineering temperature-dependent carrier concentration in bulk composite materials via temperature-dependent Fermi level offset